Probing photoinduced electron-transfer in graphene-dye hybrid materials for DSSC

Guarracino, Paola; Gatti, Teresa; Canever, Nicolo; Abdu-Aguye, Mustapha; Loi, Maria Antonietta; Menna, Enzo; Franco, Lorenzo

Published in:
PPCP : Physical Chemistry Chemical Physics

DOI:
10.1039/c7cp04308b

Publication date:
2017

PCCP

PAPER

View Article Online
View Journal | View Issue

Cite this: *Phys. Chem. Chem. Phys.*, 2017, **19**, 27716

Probing photoinduced electron-transfer in graphene–dye hybrid materials for DSSC†

Paola Guarracino,[a] Teresa Gatti,[a] Nicolò Canever,[a] Mustapha Abdu-Aguye,[b] Maria Antonietta Loi,[b] Enzo Menna[a] and Lorenzo Franco*[a]

Received 27th June 2017,
Accepted 20th September 2017

DOI: 10.1039/c7cp04308b

rsc.li/pccp

We investigated the photophysical properties of a newly synthesized hybrid material composed of a triphenylamine dye covalently bound to reduced graphene oxide, potentially relevant as a stable photosensitizer in dye-sensitized solar cells. The photophysical characterization has been carried out by means of fluorescence quenching and fluorescence lifetime measurements, complemented by Electron Paramagnetic Resonance (EPR) spectroscopy, aimed at the detailed description of the photoinduced processes occurring in the hybrid and in the mixed hybrid/N-doped TiO_2 material. The combined optical/magnetic study unequivocally demonstrates a fast quenching of the dye excited state in the isolated hybrid and an efficient electron transfer to N-doped titania nanopowders. In the latter case, a metastable radical cation on the dye moiety is photogenerated and the corresponding negative charge, an electron, is trapped in defect sites of the doped semiconductor oxide. The spin distribution in the stable radical has been determined by EPR spectroscopy and correlated with DFT calculations.

Introduction

Over the past decades, great research efforts have been focused on the development and improvement of the so-called 'third-generation photovoltaics' technology.[1–3] So far, several device architectures have been studied involving various kinds of organic/hybrid photoactive materials with the aim of reducing the costs and the environmental impact of conventional Silicon photovoltaics (PV) and approaching new applications by virtue of the light-weight and flexibility of the new materials. Organic and hybrid architectures include perovskite solar cells (PSC), that reached efficiencies higher than 20%[4–6] but suffer from stability issues,[7,8] and include other devices based on polymer bulk-heterojunction solar cells (BHJSC) and dye-sensitized solar cells (DSSC). Current research on these PV systems is focused both on the improvement of the photoactive materials, relying on a deeper understanding of their photophysical properties, and on the optimization of the device architectures.

Triphenylamine-based dyes (TPA) are versatile photoactive components that have been successfully employed in a number of organic/hybrid PV cells, including small-molecule solar cells (in blends with PCBM), DSSC and PSC.[9–11] Remarkable power conversion efficiencies (PCE) were achieved for the cited architectures using TPA-based materials, namely 11% PCE for small-molecule solar cells, and more than 14% and 20% PCE for DSSC and PSC respectively, employing TPAs as sensitizers (in DSSC) or as Hole-Transport Materials (in PSC).[12–14] TPAs are particularly important for DSSC, where they are used as alternatives to Ru complexes, in the so-called metal-free DSSC. The most useful properties of TPA are the strong electron-donating capability, due to low ionization potential, the ease of chemical modification to properly adjust their electronic properties, and the good hole-transport ability. For these reasons, the TPA moiety is usually employed as an electron-donating unit in D–π–A chromophores, where a conjugated bridge links the TPA to the acceptor group that also acts as an anchoring group for the semiconductor surface.[15] Such architecture allows extending the spectral absorption to longer wavelengths and to enhance charge injection by virtue of the intramolecular charge separation (push–pull effect).

Graphene emerged in the 2000s as a 2D-material with fascinating properties.[16] Several features make it a promising material for application to energy conversion devices: its flexibility, the large surface area, the chemical stability and the excellent electron mobility (approaching 10^4 cm^2 V^{-1} s^{-1} at room temperature[17]). Reduced graphene oxide (rGO), obtained by chemical reduction of graphene oxide (GO), is more commonly used because of its easier large-scale production compared to graphene.[18] So far, rGO has been employed in BHJSC, DSSC and PSC with encouraging results.[7,19–27] In DSSC, rGO proved

[a] *Department of Chemical Sciences, University of Padova, Via Marzolo 1, 35131 Padova, Italy. E-mail: lorenzo.franco@unipd.it*
[b] *Photophysics and OptoElectronics, Zernike Institute of Advanced Materials, Rijksuniversiteit Groningen, Nijenborgh 4 NL-9747 AG, Groningen, The Netherlands*

† Electronic supplementary information (ESI) available: Details about the synthetic route and thermogravimetric analysis, additional electron paramagnetic resonance data. See DOI: 10.1039/c7cp04308b

to be a good alternative to the ITO and FTO transparent conductive layers as well as to the Pt counter electrode[19] and was used in blend with TiO_2 to improve the conductivity of the semiconductor.[24] Several examples of the use of rGO in photoactive materials rather than in electrodes, are found in the field of BHJSC, where it was mainly used as electron acceptor material in blends with conjugated donor polymers.[22,28]

A covalent rGO–metallopolymer hybrid was developed by Fang *et al.*[25] exhibiting enhanced PCE when blended with PCBM compared to that of the ungrafted metallopolymer. More generally, the concept of a hybrid material, where an organic dye is covalently attached to rGO sheets, has been explored in the last few years, revealing positive effects from the presence of rGO, such as the enhanced conductivity and the greater stability of the hybrid material.[21,29–31]

In light of the acknowledged properties of triphenylamine-based dyes and rGO, we recently synthesized and demonstrated the efficacy of a TPA–rGO covalent hybrid for specific use as a photosensitizer in DSSC.[32]

With these premises, the scope of the present study was to gain deeper knowledge of the photophysics of the TPA–rGO hybrid material, free or adsorbed on N-doped TiO_2, starting from a model system, depicted in Chart 1, where the chromophore consists of ethyl cyanoacrylate-functionalized triphenylamine (TPA-Et) grafted onto rGO (rGO–TPA-Et). Although the carboxylic group is commonly used in the dye molecule as an anchoring moiety for TiO_2, here we chose to investigate the ester derivative because of its easier processability, in particular the possibility of obtaining dispersions of the corresponding hybrid in organic solvents, making the spectroscopic characterization more accessible. The results we present here demonstrate that even the ester group enables a strong interaction with the inorganic semiconductor, thus justifying our choice. The N-doping of TiO_2 was found to provide the spectroscopic signature of the direction of the electron transfer, and since the amount of doping is in the ppb scale, we believe it does not affect significantly the photophysics of the material. Thus, we are confident that our results are valid for pure TiO_2 as well, which is commonly used in DSSC.

We focused our work on the light absorption and photoluminescence properties of the hybrid material and applied Electron Paramagnetic Resonance spectroscopy (EPR) to investigate the photoinduced charge transfer process between the hybrid and the nanoporous titania substrate.

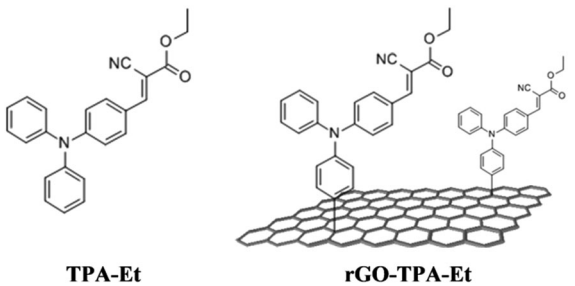

TPA-Et rGO-TPA-Et

Chart 1 Structures of the dye (TPA-Et) and hybrid material (rGO–TPA-Et) investigated.

EPR is a selective and sensitive spectroscopic method to detect paramagnetic species, and as such it is a useful technique to investigate the photoinduced processes in photovoltaic materials where organic radicals and other paramagnetic species are generated by photoinduced electron transfer.[33–35] In our case, the aim of the EPR investigation was to probe the photophysics of the hybrid system on TiO_2 and compare it to the conventional configuration of the photoactive material for DSSCs *i.e.* the dye TPA-Et adsorbed on TiO_2. In addition to this primary interest, we applied EPR to the characterization of the spin distribution in the dye radical cation that was supported by DFT calculations. This also provided us with a distinctive mark of the species that might be generated in the photovoltaic material by photoinduced electron transfer. We then investigated the dye/TiO_2 and rGO–TPA-Et/TiO_2 photogeneration of paramagnetic species. From the results, we could identify the preferred route for electron transfer in the presence of the semiconductor substrate.

Materials and methods

All reagents and solvents were purchased from Sigma-Aldrich and used as received. Reduced graphene oxide (rGO) powder was purchased from ACS Material, LLC (product no: GnP1L-0.5g) and used as received. The production method, as reported by the supplier, consists in completely reducing graphene oxide obtained *via* the Hummer's method through thermal exfoliation reduction and further hydrogen reduction. The reduced graphene oxide flakes having lateral dimensions between 1 and 2 μm, are constituted of a few layers overlapping irregularly and have many corrugations, as evident from transmission electron microscopy (TEM) images (see ref. 7).

Synthesis and characterization of rGO–TPA-Et

The synthesis of the model TPA-Et dye was adapted from a literature procedure.[15] The synthetic route towards the diazonium derivative of the TPA-Et dye (BF_4^-–N_2^+–TPA-Et), required for the functionalization of rGO, is described in the ESI,† together with all the synthetic procedures relative to each step of the route. Here we report only the procedure for rGO functionalization (a scheme of this reaction is included in Scheme SI-1, ESI†).

A suspension of rGO (10 mg, 0.83 mmol of C) in *N*-cyclohexylpirrolidone (CHP, 7 mL) was prepared by pulsed sonication (power level: 2.0, pulse on: 3 s, pulse off: 3 s, effective time: 10 min) using a Misonix 3000 titanium tip sonicator. This suspension was directly added to a solution of the freshly obtained diazonium salt BF_4^-–N_2^+–TPA-Et (429.2 mg, 0.89 mmol) in CHP (3 mL), cooled in an ice bath. The mixture was stirred at room temperature for 15′, after which methanol (100 mL) was added to precipitate the product. The reaction mixture was filtered on a Millipore® Fluoropore® membrane, and the filtrate washed thoroughly with DMF and then with MeOH until the washings were colorless, to make sure that all the unreacted diazonium salt and other possible species formed during the reaction and not covalently attached to the rGO surface were removed. The membrane was dried under an IR lamp for 15 minutes.

The functionalized rGO was then recovered by sonicating the Fluoropore® membrane in 7 mL of DMF (power level: 2.0, pulse on: 3 s, pulse off: 3 s, effective time: 1 min), centrifuging the resulting dispersion (3000 rpm, 3 min), and removing the supernatant. Ultracentrifugation was performed on an MR23i Jouan ultracentrifuge equipped with a SWM 180.5 swinging bucket rotor (Thermo Electron Corporation). The product was isolated as a dark powder after drying under vacuum.

The effective amount of TPA-Et functionalities covalently attached to the rGO surface after the diazotization reaction was determined *via* TGA analysis, following the procedure previously described,[7] using a Q5000IR TGA (TA Instruments) under nitrogen with an isotherm at 100 °C for 10 min followed by heating at 10 °C min^{-1} rate until 1000 °C. A functionalization degree (FD) of 1/62 was found for the rGO–TPA-Et dyad, meaning that one TPA-Et residue is present on average for every 62 carbon atoms of the rGO backbone (see Fig. SI-1 in the ESI† for the corresponding thermogram). The average dimension of the rGO–TPA-Et hybrid was determined through dynamic light scattering (DLS) measurements of the dyad dispersed in air-equilibrated dimethylformamide (DMF), performed with a Zetasizer Nano S (Malvern Instruments) at 20 °C setting 20 runs of 10 seconds for each measurement (quartz cuvettes with a 10 mm optical path were used). The analysis furnished a single solvodynamic diameter distribution centered around 460 nm, a value perfectly compatible with the dimensions of individual, non-aggregated particles of rGO–TPA-Et dispersed in DMF.

Absorption and photoluminescence spectroscopy

Absorption spectra were registered with a Varian Cary 5000 spectrophotometer. Steady-state photoluminescence spectra were collected *via* a spectrometer with a grating of 50 lines per mm and recorded with a Hamamatsu EM-CCD camera sensitive in the visible region. For time resolved measurements, spectra were collected on a Hamamatsu streak camera working in synchroscan mode (time resolution ~2 ps) with a cathode also sensitive in the visible region. All spectra were corrected for the response of the setup using a calibrated lamp.

Photoluminescence measurements were carried out in quartz cuvettes with 2 mm path length. Samples were dispersed in DMF and those containing rGO were sonicated at low power for a few minutes to ensure good dispersion. The excitation source was the second harmonic (approximately 400 nm) of a mode-locked Ti:sapphire laser delivering 150 fs at a repetition rate of 76 MHz. The excitation beam was spatially limited by an iris and power was adjusted using neutral density filters. For time resolved measurements, the same pulsed excitation was used.

Details about computational analysis

DFT calculations on the ground-state and oxidized radical species were performed using the Gaussian 09 program[36] with the B3LYP functional and 6-31G* basis set for both the geometry optimization and the single point energy calculation. This level of theory was chosen on the basis of a previous study on ^{14}N-containing aromatic radicals, showing that the B3LYP/6-31G* combination leads to better prediction of the EPR parameters and spin density distribution compared to higher levels of theory.[37]

EPR spectroscopy

Oxidation of TPA-Et in toluene solution (1 mM) was carried out using an excess of the oxidant [bis(trifluoroacetoxy)iodo]benzene (PIFA, Aldrich, used as received). The TPA-Et–TiO_2 sample for the EPR measurements was prepared by dispersing 100 mg of TiO_2 powder (Aldrich, anatase, nanopowder $d < 25$ nm) in 3 mL of a TPA-Et solution (1 mM in toluene : MeOH 1 : 1) and sonicating for two hours. The dispersion was then decanted and the supernatant was removed. The powder was dried under a nitrogen flux and put in an EPR tube that was sealed under vacuum. The same procedure was used to prepare the hybrid rGO–TPA-Et–TiO_2 sample.

Light-induced EPR measurements were performed on an X-band (9.6 GHz) Bruker ER200D spectrometer, equipped with a nitrogen-flow variable temperature system (Bruker BVT2000), for sample temperature control from 130 K to 300 K. The photoexcitation of the EPR samples was obtained using the white light from a 300 W Xe lamp, IR filtered and focused into a quartz optical fiber bringing the light to the sample inside the cavity of the EPR spectrometers. The resulting irradiation spectral range extends from about 350 nm up to 900 nm, with an intensity of about 50 mW cm^{-2}. EPR spectral simulations were performed using Easyspin, a Matlab Toolbox.[38]

Results and discussion

Synthesis and optical characterization

The envisaged synthetic strategy for the covalent anchoring of the TPA-Et dye moiety to the surface of rGO is the diazotization reaction, also called Tour reaction.[39,40] The rGO functionalization was carried out making use of a suitable diazonium salt derivative of TPA-Et, namely the tetrafluoroborate BF_4^-–N_2^+–TPA-Et, prepared from the corresponding aniline precursor and stable under ambient conditions (see ESI† for details about the synthesis). The addition of BF_4^-–N_2^+–TPA-Et to rGO was performed at room temperature in CHP (see Scheme SI-1, ESI†), the best solvent to disperse rGO flakes.[41] Repeated washings of the resulting material with DMF and methanol ensured the complete elimination of non-covalently bound TPA-Et species.

The rGO–TPA-Et covalent hybrid was characterized by UV-visible-NIR spectroscopy, steady-state and time-resolved photoluminescence (ST-PL and TR-PL) in comparison with the model TPA-Et dye. The resulting spectra are reported in Fig. 1.

The absorption features of the covalent dyad are characterized by two contributions: a continuous band spreading from the UV to the NIR range due to the presence of rGO and a band emerging in the visible range due to the TPA-Et dye (see Fig. 1a). The dyad has a maximum at 409 nm, whereas the free TPA-Et dye, characterized by a similar absorption band, shows a maximum at 406 nm. The 3 nm bathochromic shift of the dye absorption maximum in the hybrid is a clear proof of the covalent binding of the small molecule to the surface of the carbon nanostructure, as was demonstrated previously by us and by other authors.[32,42]

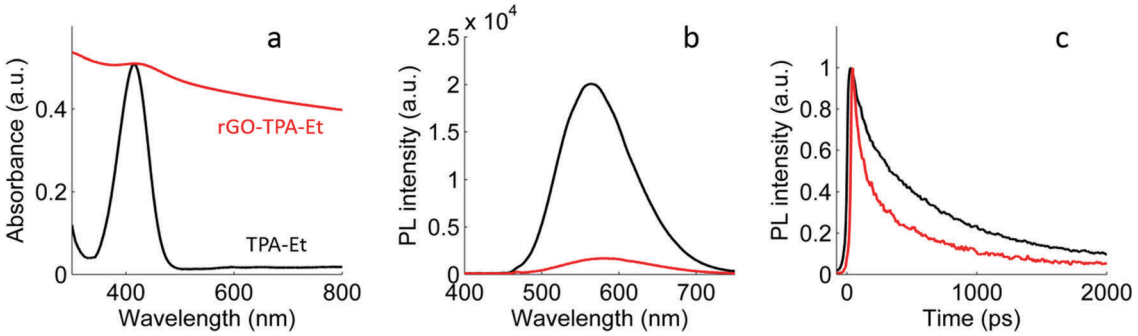

Fig. 1 (a) UV-visible-NIR absorption spectra of the pristine TPA-Et dye (black) and of the rGO–TPA-Et covalent dyad (red), (b) corresponding ST-PL spectra (λ_{exc} = 400 nm, P = 75 μW) and (c) TR-PL spectra (λ_{exc} = 400 nm, P = 75 μW) in DMF.

The ST-PL of the iso-absorbing solutions of the graphene–dye covalent hybrid and of the free dye at 400 nm were measured, showing a pronounced quenching of the emission of the TPA-Et unit when bound covalently to rGO (Fig. 1b). This behaviour indicates that processes of energy/electron transfer might take place from the dye to graphene following photo-excitation of the former. The TR-PL further confirms this observation with a faster PL decay from the functionalized rGO sample compared to that of the pristine TPA-Et dye (Fig. 1c). The PL decay was fit with a biexponential decay function: $y(t) = A_1 \exp(t/\tau_1) + A_2 \exp(t/\tau_2)$ where the lifetimes are represented by τ_n and their corresponding weights are represented by A_n. The pristine dye exhibits photoluminescence decay with lifetimes of 158 ps/1012 ps respectively. When it is attached to rGO, the photoluminescence lifetime is reduced to 83 ps/831 ps.

DFT calculations

We carried out DFT calculations on TPA-Et and on a rGO–TPA-Et model system in which the TPA-Et moiety bears a methyl group with three vinyl substituents in *para*-position of one phenyl ring (mimicking the interaction with rGO sp^2 carbon atoms). This model was already employed by us in other cases and revealed to be consistent enough to rule out the contribution of the carbon nanostructure to the molecular orbitals and energy levels of the covalently bound chromophore.[32,43] In particular, inspection of the frontier molecular orbitals in both the rGO–dye model and TPA-Et (Fig. SI-2, ESI†) shows that the HOMO is mainly localized on the TPA unit (which is reasonable in a D–A system containing TPA donor units) with partial delocalization on the vinyl groups. The LUMO in both cases is positioned on the cyanoacrylic moiety, as expected for the D–A system. In addition, the HOMO of the rGO–TPA-Et model results slightly shifted to higher energies compared to the TPA-Et reference compound (−5.39 eV *vs.* −5.19 eV) while the LUMO energy is unchanged (−2.18 eV). This is a sign that an electron donating unit has been introduced and is in agreement with the slight red shift that is observed in the absorption maximum.

B3LYP/6-31G* DFT calculations were performed also on both the oxidized TPA-Et and rGO–TPA-Et model system. The results predict that the 90.5% of the spin density (unpaired electron density) of the TPA-Et$^{\bullet+}$ radical is localized on the TPA

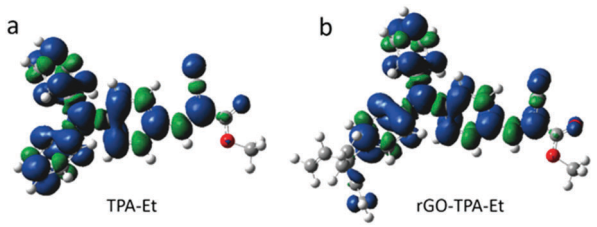

Fig. 2 Isodensity plots of the spin-density distributions calculated at the B3LYP/6-31G* level for the oxidized TPA-Et (a) and the rGO–TPA-Et model (b). The ethyl group was replaced by a methyl group for geometry optimization.

portion, as shown by the spin-density isosurface plot reported in Fig. 2a. This is reflected by the computed isotropic hyperfine coupling constants (a_{iso}), directly depending on the spin density at the nuclear position of magnetic nuclei having the highest values for the aminic ^{14}N and the aromatic protons in the *para* positions (Table 1).

The methine proton and cyano ^{14}N have consistently lower a_{iso} values, due to the scarce electron delocalization over this portion of the molecule. Such a spin-density distribution in the D–A chromophore is expected to be beneficial for the performance of the DSSC since the unpaired spin is expected to be spatially separated from the anchoring group and therefore from the TiO_2 surface, thus hindering the back-electron transfer from the semiconductor towards the sensitizer.

The rGO–TPA-Et model system shows essentially the same characteristics of the spin distribution compared to the free dye, with little spin delocalization over the vinyl groups (Fig. 2b) causing a small reduction of the hyperfine constants in the TPA moiety (Table 1).

EPR measurements

We applied EPR spectroscopy to gain more insight into the photophysics of the dye–graphene hybrid and to investigate the processes occurring when the composite is adsorbed on N-doped TiO_2, comparing them to those of the dye–TiO_2 blend.

The toluene solutions of the hybrid rGO–TPA-Et and of a mixture of rGO and TPA-Et were studied by EPR under white light photoexcitation in an attempt to clarify the nature of the PL quenching observed for the hybrid. Indeed, the observed PL

Table 1 Experimental isotropic g-factor and hyperfine coupling constants derived from the simulation of the TPA-Et radical cation EPR spectrum in solution (Fig. 3a) and calculated hyperfine constants using the B3LYP/6-31G* DFT method for both the TPA-Et and the rGO–TPA-Et radicals. The experimental values are given with an estimated error of about ±0.05 Gauss

			$\lvert a_{iso}\rvert$ (Gauss)				
		g_{iso}	^{14}N amine	^{14}N cyano	^{1}H *para*	^{1}H *ortho*	^{1}H *meta*
TPA-Et$^{\bullet+}$	Experimental	2.0028	8.5	1.0	2.89	2.19	1.26
TPA-Et$^{\bullet+}$	Calculated	2.0031	7.74	0.50	2.83^a, 2.79^a	1.82^a, 1.77^a, 2.12^b, 2.22^b	1.05^a, 1.06^a, 1.34^b, 1.24^b
rGO–TPA-Et$^{\bullet+}$	Calculated	2.0031	7.56	0.43	2.55	1.67^a, 2.03^b, 2.21^c, 1.61^c	1.05^a, 1.29^b, 1.05^c, 0.94^c

^{a} Hydrogens in the aromatic rings that are not substituted. ^{b} Hydrogens in the phenyl ring linked to the cyanoacrylic group. ^{c} Hydrogens in the aromatic ring attached to rGO.

quenching in the presence of rGO may be accounted for by two different processes: an energy transfer or an electron transfer, both already identified in other chromophore/graphene systems.[21] In the hybrid and in the mixture solution, no EPR spectra could be detected (either at ambient temperature or at T = 130 K) under photoexcitation. This result can be explained either by a very low efficiency of electron transfer from the dye to graphene or by an electron transfer to rGO followed by a fast charge recombination promoted by the high electron mobility in rGO. Indeed, a very short lifetime of the photogenerated radicals would make them undetectable by steady-state EPR.

Recently, by means of optical spectroscopic techniques, Majima *et al.* showed that electron transfer occurs on a picosecond-timescale in a dye–GO hybrid, and also demonstrated that the back electron-transfer occurs within 200 ps.[44] These data seem therefore to suggest that also in our system, without TiO_2, fast photoinduced charge separation and fast recombination occur between TPA-Et and rGO. This is consistent with the energy level arrangement of the two components as the LUMO of the dye is higher in energy than the rGO work function: the rGO work function is estimated to be −4.4 eV[24] while the LUMO level of the dye is close to −2.18 eV according to our DFT calculation.

The EPR spectrum of the TPA-Et radical cation in solution was characterized before proceeding to the analysis of the hybrid–TiO_2 and dye–TiO_2 blends. The aim of this investigation was to obtain a spectrum of the cation that we expect to form in the photoexcited blends and to analyse its spin distribution. The radical cation was obtained in toluene solution using the hypervalent iodine oxidant [bis(trifluoroacetoxy)iodo]benzene (PIFA), which is known to efficiently oxidise aromatic compounds *via* single-electron transfer[45] (Scheme SI-2, ESI†). It is noteworthy to mention that the radical cation generation was efficiently enhanced by continuous visible light illumination of the solution. In these conditions, a strong CW EPR spectrum was recorded both at ambient temperature (Fig. 3a) and in frozen solution at 130 K (Fig. 3b). The EPR pattern of both spectra is broadly structured into three lines, due to the hyperfine interaction between the unpaired electron and a spin I = 1 nucleus, which is to be assigned to a ^{14}N nucleus. The spectral fitting of the frozen solution spectrum (Fig. 3b) was obtained by considering the hyperfine interaction with a single ^{14}N atom, with the principal values A_x = 0.7 G, A_y = 5 G and A_z = 21.5 G. Based on DFT calculations, the ^{14}N giving rise to this hyperfine interaction should be identified with the amine nitrogen, since the computed unpaired spin

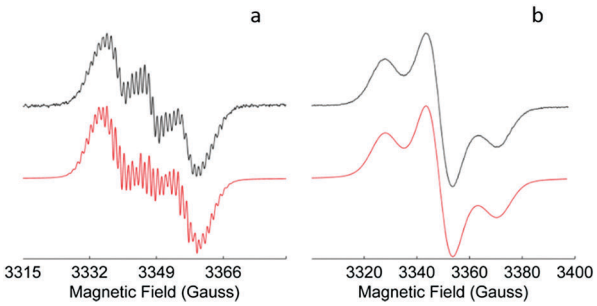

Fig. 3 Black lines: experimental EPR spectra of the TPA-Et radical cation in toluene. (a) Liquid toluene solution, T = 298 K. (b) Frozen toluene solution, T = 130 K. Red lines: simulated spectra using the parameters indicated in the text and in Table 1.

density is mostly localized on the triphenylamine moiety. Further smaller hyperfine couplings with hydrogen nuclei are unresolved in the frozen solution spectrum due to inhomogeneous broadening, but are recovered in the spectrum recorded at ambient temperature (Fig. 3a), providing an estimate of some of the isotropic hyperfine interactions.

Indeed, the EPR spectrum of the solution shows a finer structure in addition to the three-line pattern, that is attributable to the hyperfine coupling of the unpaired electron with the hydrogen nuclei and the cyano-group nitrogen. The unresolved superposition of many lines makes it difficult to extract the hyperfine constants of all the coupled nuclei. However, a reasonable estimate of the isotropic hyperfine coupling constants (a_{iso}) of the aromatic hydrogens, assuming an almost symmetrical spin density distribution among the three aromatic rings, could be achieved, leading to the spectral simulation reported in red in Fig. 3a. The resulting constants for the aromatic protons and cyano-N are reported in Table 1, together with the a_{iso} of the aminic N that is readily extracted from the spectrum.

The experimental results are in excellent agreement with the calculated a_{iso} values, confirming the reliability of the computational method. The small cyano-group ^{14}N coupling constant suggests negligible spin-density over this part of the molecule, as predicted by the calculations. Our results for a_{iso} values are in line with the reported data for the unsubstituted triphenylamine radical cation.[46,47]

The TPA-Et radical cation generated in more concentrated toluene solutions and under white light illumination, showed an EPR spectrum composed of a multiplet of five lines (Fig. SI-3, ESI†)

that we explained by the hyperfine coupling of the unpaired electron with two equivalent ^{14}N nuclei sharing the spin density in an almost symmetrical dimeric structure. This dimerization hypothesis is also supported by the value of the ^{14}N isotropic hyperfine coupling constant measured from the spectrum ($a_{iso}(N)$ = 4.1 G), which is almost exactly half of the value in the monomer, indicating a distribution of the unpaired electron into an orbital which is extended over two TPA units. Previous data on an analogous radical cation observed *via* EPR on an oxidized unsubstituted triphenylamine showed a very similar dimeric spectrum and a similar ^{14}N hyperfine coupling constant.[48] Given the observed tendency of the TPA-Et radical cation to dimerize, we suggest that the grafting of the dye on graphene can be beneficial for device performance as the immobilization of the TPA-Et on the rGO may prevent the self-dimerization and therefore the aging of the dye under operating conditions in photovoltaic devices. Moreover, the covalent bonding of TPA on rGO avoids the formation of π-stacking aggregates of the dye that might decrease the photovoltaic performances.[11]

The following step was the investigation of the TPA-Et/TiO_2 and rGO–TPA-Et/TiO_2 powders. A series of paramagnetic defects are known to be present in N-doped TiO_2 nanopowders, and some of them are well characterized in several EPR and computational studies. Among the large variety of defects, there is a subset related to nitrogen atoms incorporated in the bulk of titanium dioxide.[49–51] These species (hereafter labelled as $N_b^\bullet$ following ref. 49–51), are involved in the visible-light sensitization of the material, due to the introduction of localized states in the bandgap of the solid. We detected by EPR the same kind of paramagnetic species on our TiO_2 powder, showing an EPR spectrum coincident with the reported $N_b^\bullet$ species that increases in intensity under visible illumination (Fig. SI-4, ESI†). According to previous studies, the EPR photoresponse is explained by the promotion of electrons from localized diamagnetic states (N_b^-) to the conduction band of TiO_2, leading to the formation of additional $N_b^\bullet$ paramagnetic centers[50] (Scheme SI-3, ESI†).

The light-induced EPR spectra (light–dark) of the samples in which the TiO_2 powder was mixed with TPA-Et or rGO–TPA-Et are reported in Fig. 4. In both cases, a photoinduced EPR signal was detected. The spectra are substantially different from the photoinduced spectrum of the TiO_2 (Fig. 5 and Fig. SI-4, ESI†) and the *g*-factors of the observed lines correspond to the *g*-factor of the TPA-Et radical cation observed in frozen solution (Fig. 4 blue line). As a control experiment, we also recorded the light-induced EPR spectrum on rGO dispersed into TiO_2, where the only photoinduced signal we observed was the $N_b^\bullet$ signal of TiO_2 (Fig. SI-5, ESI†). Thus, we deduced that efficient electron transfer with formation of a stable dye radical cation is occurring both in the rGO–TPA-Et/TiO_2 and in the TPA-Et/TiO_2 systems. The lower intensity of the light-induced EPR spectrum of rGO–TPA-Et/TiO_2, leading to a smaller signal-to-noise ratio, is to be attributed to the difficulty of obtaining fine dispersions of the hybrid, limiting the dye loading of the TiO_2 semiconductor. As pointed out in our previous study,[32] this drawback may be eliminated by using rGO with smaller dimensions that should lead to more easily dispersed hybrids, interacting more efficiently with the TiO_2 semiconductor.

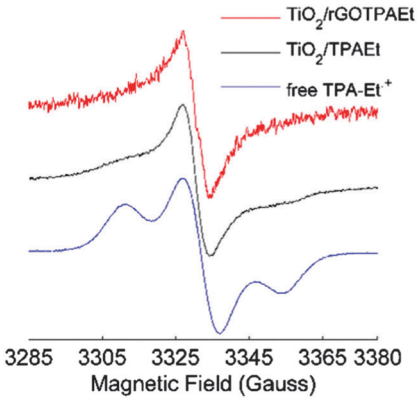

Fig. 4 Normalized EPR spectra recorded at T = 130 K of the TPA-Et/TiO_2, rGO–TPA-Et/TiO_2 and TPA-Et radical cation in frozen solution. The spectra are obtained as the difference between the spectrum recorded under white light illumination and the spectrum in the dark.

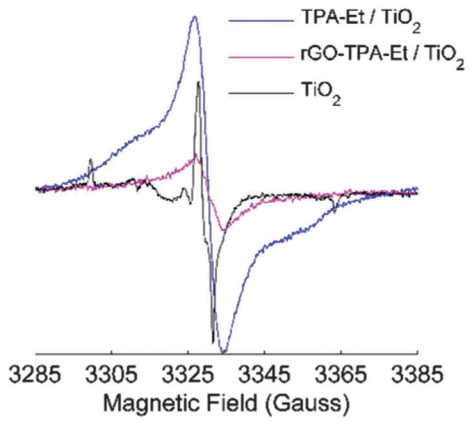

Fig. 5 Light-induced EPR spectra of the TiO_2, TPA-Et/TiO_2 and rGO–TPA-Et/TiO_2 samples (T = 130 K).

By observing the EPR spectra in Fig. 4 it is possible to note a difference in the lineshape between the TPA-$Et^{\bullet+}$ radical in solution and in the TiO_2/dye systems: the two outer bands (originating from the N hyperfine coupling) are less intense and broader in the samples with TiO_2. The reason can be attributed either to a static or dynamic phenomenon occurring in the solid blends. The static one consists in a delocalization of the TPA-Et radical spin density in more than a single molecule, causing a reduction of the hyperfine splittings and the collapse of the spectrum towards the central line. In the TPA-Et/TiO_2 blends, this phenomenon may be related to dye aggregation. In the case of rGO–TPA-Et/TiO_2, the lineshape could be explained by the occurrence of partial delocalization of the unpaired electron over the graphene network, determining the smaller hyperfine interaction with the amine nitrogen. However, we can exclude this phenomenon on the basis of our DFT calculation on the model rGO–TPA-Et radical cation, showing that the extent of unpaired spin delocalization over the graphene region is small, causing only a minor reduction of the hyperfine

constants in the amine portion (Table 1). Therefore, in the case of the hybrid adsorbed on TiO_2, we believe that the lineshape variations with respect to the free TPA-Et radical are likely related to dynamical phenomena.

The dynamic reason for the lineshape broadening in TPA-Et/TiO_2 could be described as caused by the high mobility of positive charges (holes) undergoing a hopping motion between TPA-Et molecules. If the hopping proceeds with a fast rate, a partial averaging of hyperfine couplings ensues that explains the broad lineshape. In a frozen solution of TPA-Et the solvent separating the dye molecules does not allow a significant hole motion, but in TPA-Et/TiO_2 samples, in the presence of some aggregation of the dye, a hopping motion of the hole among the adjacent TPA-Et molecules becomes feasible. A different explanation must be devised for the increased hole mobility in the rGO–TPA-Et/TiO_2 material, considering that the dye molecules anchored to the graphene surface are quite diluted, as demonstrated by TGA analysis. In this case, no direct hopping of the unpaired electron (and therefore the hole) between dyes is expected, but a charge transfer mechanism mediated by the π orbitals of graphene could be active that can effectively transfer the charges between different grafted dyes.

The comparison of the light-induced EPR spectra of pure TiO_2 and TiO_2 mixed with TPA-Et or rGO–TPA-Et reveals that the signal attributed to $N_b^\bullet$ defects vanishes in the TiO_2 stained with the dyes (Fig. 5). We explain this result by noting that the localized nitrogen paramagnetic $N_b^\bullet$ defects behave as traps for the electrons injected into the TiO_2 conduction band by the photoexcited dye. After the electron trapping, the $N_b^\bullet$ defects become diamagnetic and therefore EPR silent (eqn (1)).

$$N_b^\bullet(\text{paramagnetic}) + e^- \rightarrow N_b^-(\text{diamagnetic}) \quad (1)$$

Therefore, we exploited the intrinsic TiO_2 defects as probes to reveal the photoinduced electron injection into the TiO_2.

In conclusion, in our TPA-Et/TiO_2 and rGO–TPA-Et/TiO_2 samples, the disappearance of $N_b^\bullet$ defects and the formation of radical cations under photoexcitation unequivocally demonstrate the electron transfer from TPA-Et to the TiO_2, even in presence of the graphene hybrid as sensitizer. This result was not so expected in the hybrid rGO–TPA-Et dispersed on TiO_2, since the electron transfer from the dye to the graphene is the main process causing excitation quenching in the hybrid in solution. However, our EPR results demonstrate that when the hybrid is blended with TiO_2 the electron transfer towards TiO_2 is the most efficient process, while the electron transfer from TPA-Et to graphene is of minor importance.

As suggested in a recent paper by Rozhkova and co-workers the possibility of electron transfer from photoexcited rGO to TiO_2 should also be considered.[52] The authors demonstrated that photoexcited rGO is able to transfer electrons to the semiconductor in a Pt/TiO_2–rGO photocatalytic system by showing that the EPR signal of rGO electrons is lowered upon illumination and a Ti^{3+} signal arises. However, our EPR measurements do not show this behaviour, suggesting that the phenomenon observed by Rozhkova may be influenced by the presence of the Pt cocatalyst by the rGO production method and the mixed rutile/anatase nanopowder used. Indeed, although in our case a clear observation of the rGO signal variation is hampered by the presence of the overlapping (and larger) line of the TPA-Et radical in rGO–TPA-Et/TiO_2 and of the $N_b^\bullet$ defects in rGO/TiO_2, we observed the same increase of the $N_b^\bullet$ EPR signal in the illuminated rGO/TiO_2 blend (see Fig. SI-4, ESI†) as in neat TiO_2. This means that rGO does not transfer electrons to the semiconductor as they would be trapped in $N_b^\bullet$ defects making them diamagnetic and quenching their EPR signal. In our case, the lack of a photoinduced signal of Ti^{3+} would be a further confirmation of the absence of electron transfer from rGO to TiO_2, but it must be noted that the detection of the EPR spectrum of Ti^{3+} usually requires sample temperatures lower than those used in our work.

According to this description of the photophysics of the material and considering that the rGO work function lies higher in energy compared to the HOMO of the dye (−5.39 eV), we suggest that the rGO should be able to efficiently reduce the oxidized TPA-Et, potentially aiding the regeneration of the active chromophore in an operating DSSC device.

Conclusions

We synthesized the rGO–TPA-Et hybrid as a model sensitizer for DSSCs, and explored the photoinduced processes occurring in the material either alone or adsorbed on N-doped TiO_2 nanopowders, making a comparison with the free dye TPA-Et. We employed both optical (absorption and emission spectroscopy) and magnetic (EPR) spectroscopic techniques for this purpose.

From the optical measurements on the dye and hybrid solutions, a quenching of the dye photoluminescence was observed when it is bound to rGO. We performed light-induced EPR experiments on the hybrid in solution using visible-light excitation, which failed to identify the formation of a stable radical cation of the dye. The absence of a stable radical cation is explained, following previous suggestions, with the occurrence of a fast photoinduced electron transfer from the dye to rGO and subsequent fast recombination.

In contrast, when the dye or the hybrid were dispersed in N-doped TiO_2, we detected a strong light-induced EPR spectrum of the dye cation radical and the quenching of the nitrogen-related paramagnetic defects of the oxide. The two pieces of evidence clearly demonstrate that in the dye/TiO_2 or the rGO–dye/TiO_2 mixed materials an efficient photoinduced electron transfer from the excited dye to the conduction band of the oxide is active, generating a persistent radical cation of the dye.

The rGO–dye architecture seems therefore to be applicable to DSSC as the main requirements for TiO_2 sensitization are fulfilled, although further improvements concerning the solubility of the hybrid and its efficiency in staining the TiO_2, should be explored. Furthermore, the effect of the rGO on the dye-regeneration is promising, as the material could be an effective redox mediator.

Conflicts of interest

There are no conflicts of interest to declare.

Acknowledgements

Financial support from Centro Studi di Economia e Tecnica dell'Energia Giorgio Levi Cases of the University of Padova is gratefully acknowledged (project OPERA). We also thank Widianta Gomulya and Simon Kahmann for help with the PL measurements.

References

1 J. Yan and B. R. Saunders, *RSC Adv.*, 2014, **4**, 43286–43314.
2 L. Lu, T. Zheng, Q. Wu, A. M. Schneider, D. Zhao and L. Yu, *Chem. Rev.*, 2015, **115**, 12666–12731.
3 S. Thomas, T. G. Deepak, G. S. Anjusree, T. A. Arun, S. V. Nair and A. S. Nair, *J. Mater. Chem. A*, 2014, **2**, 4474–4490.
4 M. A. Green, K. Emery, Y. Hishikawa, W. Warta and E. D. Dunlop, *Prog. Photovoltaics*, 2016, **24**, 905–913.
5 W. Nie, H. Tsai, R. Asadpour, J.-C. Blancon, A. J. Neukirch, G. Gupta, J. J. Crochet, M. Chhowalla, S. Tretiak, M. A. Alam, H. Wang and A. D. Mohite, *Science*, 2015, **347**, 522–525.
6 D. P. McMeekin, G. Sadoughi, W. Rehman, G. E. Eperon, M. Saliba, M. T. Horantner, A. Haghighirad, N. Sakai, L. Korte, B. Rech, M. B. Johnston, L. M. Herz and H. J. Snaith, *Science*, 2016, **351**, 151–155.
7 T. Gatti, S. Casaluci, M. Prato, M. Salerno, F. Di Stasio, A. Ansaldo, E. Menna, A. Di Carlo and F. Bonaccorso, *Adv. Funct. Mater.*, 2016, **26**, 7443–7453.
8 T. A. Berhe, W.-N. Su, C.-H. Chen, C.-J. Pan, J.-H. Cheng, H.-M. Chen, M.-C. Tsai, L.-Y. Chen, A. A. Dubale and B.-J. Hwang, *Energy Environ. Sci.*, 2016, **9**, 323–356.
9 M. Liang, W. Xu, F. Cai, P. Chen, B. Peng, J. Chen and Z. Li, *J. Phys. Chem. C*, 2007, **111**, 4465–4472.
10 J. Wang, K. Liu, L. Ma and X. Zhan, *Chem. Rev.*, 2016, **116**, 14675–14725.
11 S. P. Singh, M. S. Roy, K. R. J. Thomas, S. Balaiah, K. Bhanuprakash and G. D. Sharma, *J. Phys. Chem. C*, 2012, **116**, 5941–5950.
12 X. Che, X. Xiao, J. D. Zimmerman, D. Fan and S. R. Forrest, *Adv. Energy Mater.*, 2014, **4**, 1400568.
13 K. Kakiage, Y. Aoyama, T. Yano, K. Oya, J. Fujisawa and M. Hanaya, *Chem. Commun.*, 2015, **51**, 15894–15897.
14 W. S. Yang, J. H. Noh, N. J. Jeon, Y. C. Kim, S. Ryu, J. Seo and S. I. Seok, *Science*, 2015, **348**, 1234–1237.
15 D. P. Hagberg, T. Marinado, K. M. Karlsson, K. Nonomura, P. Qin, G. Boschloo, T. Brinck, A. Hagfeldt and L. Sun, *J. Org. Chem.*, 2007, **72**, 9550–9556.
16 A. K. Geim and K. S. Novoselov, *Nat. Mater.*, 2007, **6**, 183–191.
17 K. S. Novoselov, A. K. Geim, S. V. Morozov, D. Jiang, Y. Zhang, S. V. Dubonos, I. V. Grigorieva and A. A. Firsov, *Science*, 2004, **306**, 666–669.
18 F. Bonaccorso, Z. Sun, T. Hasan and A. C. Ferrari, *Nat. Photonics*, 2010, **4**, 611–622.
19 F. Bonaccorso, L. Colombo, G. Yu, M. Stoller, V. Tozzini, A. C. Ferrari, R. S. Ruoff and V. Pellegrini, *Science*, 2015, **347**, 12465011.
20 J. D. Roy-Mayhew and I. A. Aksay, *Chem. Rev.*, 2014, **114**, 6323–6348.
21 H. X. Wang, Q. Wang, K. G. Zhou and H. L. Zhang, *Small*, 2013, **9**, 1266–1283.
22 Z. Liu, Q. Liu, Y. Huang, Y. Ma, S. Yin, X. Zhang, W. Sun and Y. Chen, *Adv. Mater.*, 2008, **20**, 3924–3930.
23 Z. Yin, S. Sun, T. Salim, S. Wu, X. Huang, Q. He, Y. M. Lam and H. Zhang, *ACS Nano*, 2010, **4**, 5263–5268.
24 Y. Tang, C.-S. Lee, J. Xu, Z. Liu, Z.-H. Chen, Z. He, Y. Cao, G. Yuan, H. Song, L. Chen, L. Luo, H.-M. Cheng, W.-J. Zhang, I. Bello and S.-T. Lee, *ACS Nano*, 2010, **4**, 3482–3488.
25 Z. Fang, A. Ito, A. C. Stuart, H. Luo, Z. Chen, K. Vinodgopal, W. You, T. J. Meyer and D. K. Taylor, *ACS Nano*, 2013, **7**, 7992–8002.
26 K. T. Cho, G. Grancini, Y. Lee, D. Konios, S. Paek, E. Kymakis and M. K. Nazeeruddin, *ChemSusChem*, 2016, **9**, 3040–3044.
27 A. L. Palma, L. Cinà, S. Pescetelli, A. Agresti, M. Raggio, R. Paolesse, F. Bonaccorso and A. Di Carlo, *Nano Energy*, 2016, **22**, 349–360.
28 Y. Wang, D. Kurunthu, G. W. Scott and C. J. Bardeen, *J. Phys. Chem. C*, 2010, **114**, 4153–4159.
29 J. Zhu, Y. Li, Y. Chen, J. Wang, B. Zhang, J. Zhang and W. J. Blau, *Carbon*, 2011, **49**, 1900–1905.
30 M.-E. Ragoussi, J. Malig, G. Katsukis, B. Butz, E. Spiecker, G. de la Torre, T. Torres and D. M. Guldi, *Angew. Chem., Int. Ed.*, 2012, **51**, 6421–6425.
31 Y. Xu, Z. Liu, X. Zhang, Y. Wang, J. Tian, Y. Huang, Y. Ma, X. Zhang and Y. Chen, *Adv. Mater.*, 2009, **21**, 1275–1279.
32 T. Gatti, N. Manfredi, C. Boldrini, F. Lamberti, A. Abbotto and E. Menna, *Carbon*, 2017, **115**, 746–753.
33 V. Dyakonov, G. Zoriniants, M. Scharber, C. J. Brabec, R. A. J. Janssen, J. C. Hummelen and N. S. Sariciftci, *Phys. Rev. B: Condens. Matter Mater. Phys.*, 1999, **59**, 8019–8025.
34 J. Behrends, A. Sperlich, A. Schnegg, T. Biskup, C. Teutloff, K. Lips, V. Dyakonov and R. Bittl, *Phys. Rev. B: Condens. Matter Mater. Phys.*, 2012, **85**, 125206.
35 L. R. Weiss, S. L. Bayliss, F. Kraffert, K. J. Thorley, J. E. Anthony, R. Bittl, R. H. Friend, A. Rao, N. C. Greenham and J. Behrends, *Nat. Phys.*, 2017, **13**, 176–182.
36 M. J. Frisch, G. W. Trucks, H. B. Schlegel, G. E. Scuseria, M. A. Robb, J. R. Cheeseman, G. Scalmani, V. Barone, B. Mennucci, G. A. Petersson, H. Nakatsuji, M. Caricato, X. Li, H. P. Hratchian, A. F. Izmaylov, J. Bloino, G. Zheng, J. L. Sonnenberg, M. Hada, M. Ehara, K. Toyota, R. Fukuda, J. Hasegawa, M. Ishida, T. Nakajima, Y. Honda, O. Kitao, H. Nakai, T. Vreven, J. A. Montgomery, Jr., J. E. Peralta, F. Ogliaro, M. Bearpark, J. J. Heyd, E. Brothers, K. N. Kudin, V. N. Staroverov, R. Kobayashi, J. Normand, K. Raghavachari, A. Rendell, J. C. Burant, S. S. Iyengar, J. Tomasi, M. Cossi, N. Rega, J. M. Millam, M. Klene, J. E. Knox, J. B. Cross, V. Bakken, C. Adamo, J. Jaramillo, R. Gomperts, R. E. Stratmann, O. Yazyev, A. J. Austin, R. Cammi, C. Pomelli, J. W. Ochterski, R. L. Martin, K. Morokuma, V. G. Zakrzewski, G. A. Voth, P. Salvador, J. J. Dannenberg, S. Dapprich, A. D. Daniels, Ö. Farkas, J. B. Foresman, J. V. Ortiz, J. Cioslowski and D. J. Fox, *Gaussian 09*, Gaussian, Inc., Wallingford CT, 2009.

37 L. Hermosilla, P. Calle and J. G. de la Vega, *RSC Adv.*, 2015, **5**, 62551–62562.
38 S. Stoll and A. Schweiger, *J. Magn. Reson.*, 2006, **178**, 42–55.
39 J. L. Bahr and J. M. Tour, *Chem. Mater.*, 2001, **13**, 3823–3824.
40 J. R. Lomeda, C. D. Doyle, D. V. Kosynkin, W. F. Hwang and J. M. Tour, *J. Am. Chem. Soc.*, 2008, **130**, 16201–16206.
41 H. Tao, Y. Zhang, Y. Gao, Z. Sun, C. Yan and J. Texter, *Phys. Chem. Chem. Phys.*, 2017, **19**, 921–960.
42 A. Setaro, P. Bluemmel, C. Maity, S. Hecht and S. Reich, *Adv. Funct. Mater.*, 2012, **22**, 2425–2431.
43 P. Salice, C. Sartorio, A. Burlini, R. Improta, B. Pignataro and E. Menna, *J. Mater. Chem. C*, 2015, **3**, 303–312.
44 T. Tachikawa, S.-C. Cui, M. Fujitsuka and T. Majima, *Phys. Chem. Chem. Phys.*, 2012, **14**, 4244.
45 T. Wirth, *Hypervalent Iodine Chemistry – Modern Developments in Organic Synthesis*, Springer-Verlag, Berlin, 2003.
46 F. Gerson and W. Huber, *Electron Spin Resonance Spectroscopy of Organic Radicals*, Wiley-VCH Verlag Gmbh & Co. KGaA, Weinheim, 2003.
47 A. Rogowska, S. Kuhl, R. Schneider, A. Walcarius and B. Champagne, *Phys. Chem. Chem. Phys.*, 2007, **9**, 828.
48 W. H. Bruning, R. F. Nelson, L. S. Marcoux and R. N. Adams, *J. Phys. Chem.*, 1967, **71**, 3055–3057.
49 S. Livraghi, M. R. Chierotti, E. Giamello, G. Magnacca, M. C. Paganini, G. Cappelletti and C. L. Bianchi, *J. Phys. Chem. C*, 2008, **112**, 17244–17252.
50 S. Livraghi, M. C. Paganini, E. Giamello, A. Selloni, C. Di Valentin and G. Pacchioni, *J. Am. Chem. Soc.*, 2006, **128**, 15666–15671.
51 C. Di Valentin, E. Finazzi, G. Pacchioni, A. Selloni, S. Livraghi, M. C. Paganini and E. Giamello, *Chem. Phys.*, 2007, **339**, 44–56.
52 P. Wang, N. M. Dimitrijevic, A. Y. Chang, R. D. Schaller, Y. Liu, T. Rajh and E. A. Rozhkova, *ACS Nano*, 2014, **8**, 7995–8002.

